Phase-dependent microstructure modification leads to high thermoelectric performance in n-type layered SnSe2

Yiqing Wei, Jingwei Li, Daliang Zhang, Bin Zhang, Zizhen Zhou, Guang Han, Guoyu Wang, Carmelo Prestipino, Pierric Lemoine, Emmanuel Guilmeau, et al.

Phase-dependent microstructure modification leads to high thermoelectric performance in *n*-type layered $SnSe_2$

Yiqing Wei [a], Jingwei Li [b], Daliang Zhang [b], Bin Zhang [c], Zizhen Zhou [a], Guang Han [d], Guoyu Wang [d], Carmelo Prestipino [e], Pierric Lemoine [f], Emmanuel Guilmeau [g], Xu Lu [a,*], Xiaoyuan Zhou [a,c,**]

[a] *Center of Quantum Materials & Devices and College of Physics, Chongqing University, Chongqing 401331, P. R. China*

[b] *Multi-scale Porous Materials Center, Institute of Advanced Interdisciplinary Studies & School of Chemistry and Chemical Engineering, Chongqing University, Chongqing, 401331, P. R. China*

[c] *Analytical and Testing Center, Chongqing University, Chongqing 401331, P. R. China*

[d] *College of Materials Science and Engineering, Chongqing University, Chongqing 400044, P. R. China*

[e] *Univ Rennes, CNRS, ISCR – UMR 6226, F-35000 Rennes, France*

[f] *Institut Jean Lamour, UMR 7198 CNRS – Université de Lorraine, 2 allée André Guinier-Campus ARTEM, BP 50840, 54011 Nancy Cedex, France*

[g] *CRISMAT, CNRS, Normandie Univ, ENSICAEN, UNICAEN, 14000 Caen, France*

** Corresponding authors: luxu@cqu.edu.cn; xiaoyuan2013@cqu.edu.cn*

Abstract

Microstructure control is crucial for thermoelectrics since it is intimately related to the scattering mechanism of both electrons and phonons. Herein, we propose a new strategy to modify microstructure by phase regulation that simultaneously induces high carrier mobility and low lattice thermal conductivity. As demonstrated in layered $SnSe_2$, the addition of Cu can induce a phase transition from space group $P\bar{3}m1$ to $P6_3mc$. Due to the enlarged formation energy of stacking faults in the later phase, the stacking fault

density is greatly reduced after heat treatment that leads to an increased grain size. Accordingly, the carrier mobility of $SnSe_{1.97}Br_{0.03}$-3% Cu sample is enhanced by 100% at room temperature. Furthermore, the reduction of stacking fault density is accompanied by the formation of pores in the matrix, which results in low lattice thermal conductivity. As a result, a record peak zT of 1.13 for $SnSe_2$-based materials is achieved at 773 K, and the attained ZT_{ave} of 0.62 is a record-high value among *n*-type polycrystalline layered materials working in intermediate-to-high temperature region. This work provides a feasible strategy to decouple the electron and phonon transport in layered thermoelectric compounds by phase-dependent microstructure modification.

Keywords

Layered compounds, Phase regulation, Stacking faults, Carrier mobility, Thermoelectrics

1. Introduction

Thermoelectric (TE) materials can convert waste heat into electricity without harmful emission, offering a promising pathway to reduce the carbon footprint [1-3]. The performance of TE materials is determined by the thermoelectric figure of merit zT, defined as $zT = S^2\sigma T/\kappa$. S and σ represent the Seebeck coefficient and electrical conductivity, respectively; T is the absolute temperature, and κ stands for the thermal conductivity consisting of lattice thermal conductivity (κ_l) and electronic thermal conductivity (κ_e). In addition to the intrinsic characteristics of materials including electronic band structures and phonon dispersion, the extrinsic factors such as different types of defects also profoundly affect the TE transport properties by inducing external scattering [4,5]. Therefore, the TE performance optimization of a certain material is closely related to the scattering of electrons and phonons [6]. In recent years, a variety of elaborate microstructures featured by rationally designed crystal defects such as point defects, line defects and planar defects have been frequently applied to strengthen

the phonon scattering for lowering κ_l to promote TE performance [7-10]. However, in most cases, the intentionally created defects would scatter electrons as well and impede the access to high TE power factor ($PF = S^2\sigma$). Thus, the competition between carrier mobility (μ) and lattice thermal conductivity makes us consider the balance between the scattering strengths of electrons and phonons when performing defect engineering on TE materials. As one typical type of planar defect, stacking faults, which can be generated by quenching, impurities, and high density of dislocations, have been utilized to reduce κ_l especially in TE materials holding cubic structure, resulting in significantly improved zT [4,11]. For example, in $Ge_{0.9}V_{0.02}Bi_{0.08}Te$ sample, high-density stacking faults can be obtained by V and Bi co-doping, leading to a low κ_l of ~0.59 W m^{-1} K^{-1} and a high zT of ~2.1 at 773 K [12]. Zou *et al*. successfully suppressed κ_l of $AgSbTe_{2-x}Se_x$ to ~0.3 W m^{-1} K^{-1} by introducing dense stacking faults to achieve a high $zT > 2$ [13]. However, as pointed out by Ziman, such planar defects not only scatter phonons but also electrons with even greater intensity, which would largely reduce carrier mobility and potentially surpass the effect of enhanced phonon scattering [14]. Therefore, we are motivated to reveal if the high density of stacking faults is always beneficial to promote the performance of other types of TE materials, and if not, how we can effectively control the density of stacking faults to optimize TE performance.

Recently, layered compounds have attracted extensive research interest in the TE field for waste heat recovery owing to their intrinsically low κ_l, as well as anisotropic phonon and electron transport properties [15-18]. Besides, some layered compounds with wide van der Waals (vdW) gaps can accommodate a variety of substances including metal atoms, MXene, and carbon based nanostructures, which would have great influence on both structure and transport properties [2,4]. The weak interlayer interaction force between vdW gaps may also lead to the occurrence of interlayer slip during the solidification process and eventually creates plenty of stacking faults. Therefore, layered compounds are suitable candidates to explore the raised question above. In fact, the carrier mobility of most layered TE compounds is greatly affected by their microstructure [19-21]. For instance, in the intensively studied SnSe, the room

temperature carrier mobility along the *b*-axis is ~250 $cm^2 V^{-1} s^{-1}$ in *n*-type single-crystal but only ~14.5 $cm^2 V^{-1} s^{-1}$ in polycrystalline *n*-type SnSe [22,23]. In contrast, the thermal conductivity of layered compounds is generally low due to the weak interlayer interactions, leaving not much room for further reduction in lattice thermal conductivity. Therefore, the planar defects in layered compounds tend to scatter electrons more strongly than phonons, which is clearly not favorable for TE performance. To this end, the core issue for the enhancement of TE performance for layered compounds is to promote a carrier mobility through diminishing planar defects.

In this work, we propose a stacking fault modulation strategy based on phase structure regulation to simultaneously tune the electron and phonon transport properties. Cu is chosen as the insertion element to be added into the $SnSe_2$ matrix, aiming to modulate its structure. As shown in Figure 1a, the addition of Cu can induce a phase transition from space group (SG) $P\bar{3}m1$ to $P6_3mc$ in $SnSe_2$. The formation of stacking faults in the $P6_3mc$ phase is more thermodynamic disadvantageous than that in the original $P\bar{3}m1$ phase, making the stacking faults in $P6_3mc$ phase more easily eliminated by heat treatment. Therefore, the density of stacking faults of $SnSe_2$ is markedly reduced in the $P6_3mc$ phase compared with the original $P\bar{3}m1$ phase, after the heat treatment (AHT) at 823 K for 20 min. Consequently, the room temperature mobility is promoted by 100% in Cu-added $SnSe_{1.97}Br_{0.03}$-AHT sample, which significantly improves electrical transport performance. At the same time, an ultra-low κ_l of 0.29 W $m^{-1} K^{-1}$ at 773 K is obtained in porous $SnSe_{1.97}Br_{0.03}$-3% Cu-AHT sample. As a result, the highest peak zT of 1.13 for $SnSe_2$-based materials (Figure 1b) is obtained in $SnSe_{1.97}Br_{0.03}$-3% Cu-AHT sample at 773 K in the out-of-plane direction [24-30]. Moreover, a record-high average ZT (ZT_{ave}) of 0.62 for *n*-type polycrystalline layered materials working in intermediate-to-high temperature region (Figure 1c) is achieved [29-36]. Here, we have unveiled the internal connection between crystal structure and micromorphology, opening a new avenue for defect engineering and an efficient way to balance carrier and phonon scattering for layered TE materials.

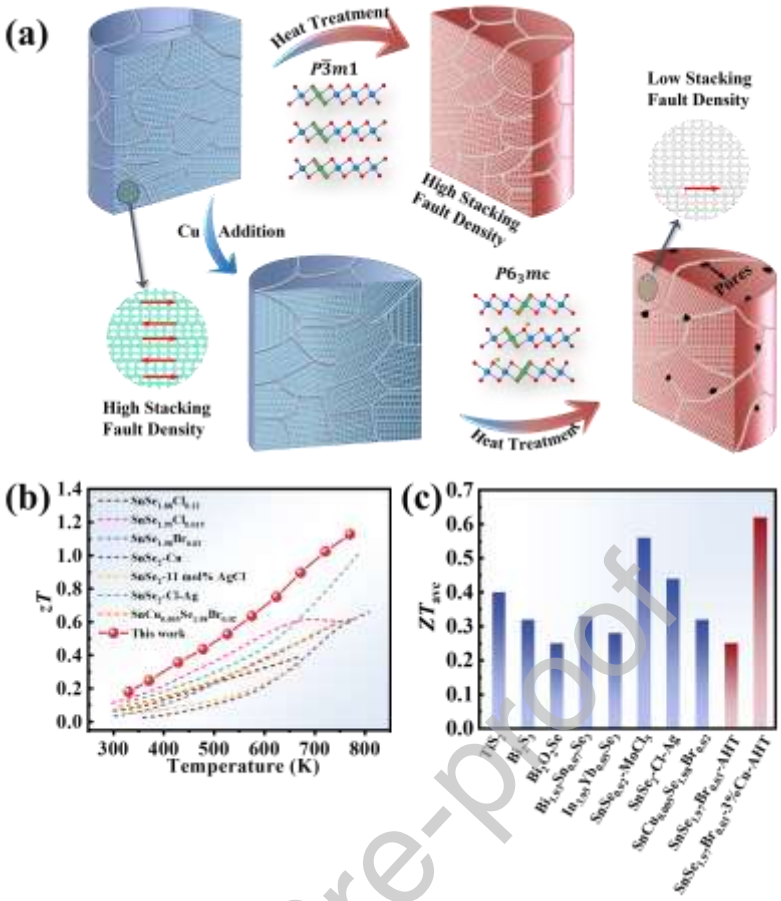

Figure 1. a) Schematic diagram showing the different crystal structures and microstructures of $SnSe_2$-based samples and the change of stacking fault density after heat treatment, b) the comparison of peak zT among $SnSe_2$-based materials [24-30], and c) the comparison of ZT_{ave} among *n*-type polycrystalline layered compounds working in intermediate-to-high temperature region [29-36].

2. Experimental Section

2.1. Synthesis

Firstly, Cu-added $SnSe_2$ powders were synthesized by a hydrothermal method. Here, CuCl (99%, Aladdin, China) powders were mixed together with Sn and Se precursors at atomic ratios of x% (x = 0, 2, 3, 4) $SnCl_2{\cdot}2H_2O$, and the remaining steps can be seen in our previous work [37]. Secondly, 5.5 g Cu-added $SnSe_2$ powders and 0.092 g $SnBr_2$ were sealed in high vacuum quartz tubes and held at 723 K for 1 h to prepare $SnSe_{1.97}Br_{0.03}$-x% Cu samples. All reagents were of analytical grade and used

directly. Finally, the as-prepared samples were consolidated into cylinders with a diameter of 10 mm using conventional hot pressing (673 K for 30 min, 50 MPa) under vacuum. The bulk samples obtained by only hot pressing are labeled as BHT samples. Afterward, the hot-pressed samples were placed in a tube furnace with Ar gas flow and heat-treated at 823 K for 20 min. The obtained samples are denoted as AHT samples. The densities (ρ) of all samples were obtained by the Archimedes method and listed in Table S2.

2.2. Characterization

Powder X-ray diffraction (XRD) patterns were collected at room temperature in Bragg-Brentano geometry using Cu Kα radiation either on PANalytical X'Pert diffractometer or Bruker D8 advance diffractometer equipped with a Ge(111) monochromator and a LynxEye detector. Rietveld refinement was performed on the XRD patterns by using either TOPAS-Academic V6 software or FullProf software included in the WinPlotr package [38,39]. The morphology characterization was performed on the scanning electron microscopy (SEM, Quattro S), where the focus is on cross sections of samples parallel to the pressure direction. In order to reveal the microstructure and elemental composition of samples, the BHT/AHT-samples were thinned along the plane parallel to the pressure direction using an ultramicrotome (Leica EM RES 102) for transmission electron microscopy (TEM, FEI Talos F200S G2) and spherical aberration-corrected scanning transmission electron microscopy (Cs-STEM, Spectra 300) characterization. Herein, the HRTEM, SAED, EDX and HAADF represent high-resolution TEM, selected area electron diffraction, energy-dispersive X-ray spectroscopy and high-angle annular dark field, respectively. Thermogravimetric analysis (TGA) was carried out to detect the thermal stability of samples from 300 K to 773 K using a thermo-gravimetric analyzer (TGA2). The averaged actual chemical composition of $SnSe_{1.97}Br_{0.03}$-3% Cu-AHT pellet was characterization by electron probe microscopic analysis (EPMA, JXA-8530 Plus Hyper Probe). $SnSe_{1.97}Br_{0.03}$-3% Cu-AHT pellet for SEM was prepared using a focused ion beam (FIB, Thermoscientific Helios 5 CX).

2.3. Transport property measurements

The BHT/AHT-samples were cut into ~1.1 mm thick discs and 2.2 mm×2.2 mm×8.5 mm rectangular blocks for measuring thermal diffusivity D on a Netzsch LFA 457 and electrical transport data on a Linseis LSR-3 parallel to the pressure direction at 323-773 K. According to the equation $\kappa = DC_p\rho$, the thermal conductivity κ can be obtained, where C_p is the heat capacity estimated by the Dulong-Petit law. n was obtained by a home-made Hall apparatus with magnetic field of 1 T from 323 K to 773 K. μ was calculated via the formula $\mu = \sigma/ne$ (σ is electrical conductivity, and e is electron charge). The estimated uncertainties of κ, σ, S, and zT are about 3%, 5%, 5% and 10%, respectively.

2.4. DFT calculations

All the first-principles calculations were implemented in the Quantum Espresso package [40]. The total energy of all the structures and the formation energy of stacking faults in different structures were calculated based on supercells containing 32 Sn atoms and 64 Se atoms, which can be used to model the results with 3% Cu addition. The lattice thermal conductivity was computed by solving the phonon Boltzmann transport equation as coded in ShengBTE program [41]. The harmonic properties were studied by density functional perturbation theory and anharmonic properties were calculated by considering three-phonon scattering and grain boundary scattering. More computational details can be seen in the SM.

3. Results and Discussion

3.1. Crystal Structure and Microstructure

As a metal dichalcogenide with a structure unit resembling MoS_2, $SnSe_2$ exhibits different crystal structures via changing the stacking forms of the monolayer counterparts [42-44]. In this work, Cu-introduced $SnSe_2$ powders were synthesized by a hydrothermal method. By comparing the phases synthesized at a relatively low temperature of 473 K by hydrothermal method, with/without the addition of Cu, it is found that the addition of Cu can induce a phase transition from the space group (SG)

$P\bar{3}m1$ to SG $P6_3mc$ in $SnSe_2$ (Figure S1a). The diffraction peaks of pristine $SnSe_2$ and solely Br-doped samples are consistent, and they can be indexed to standard card of $SnSe_2$ ($P\bar{3}m1$, PDF 89-3197) in the form of 2H-$SnSe_2$ polytype. In contrast, the collected patterns of $SnSe_2$-3% Cu sample show some redundant diffraction peaks, especially at $2\theta \sim 35°$ and 45°, which can be matched to the simulated pattern of 4H-$SnSe_2$ in the form of SG $P6_3mc$. Therefore, it is inferred that in the low temperature hydrothermal synthesis of $SnSe_2$, the composition plays important role in phase transition. As shown in Figure 2a, the two polytypes are characterized by different stacking of the Se-Sn-Se layers along the *c*-axis, and their lattice parameters are listed in Table S3. The structure of the 2H-$SnSe_2$ polytype (i.e. $P\bar{3}m1$) is formed by the stacking of the same monolayer (AAA) with a stacking vector [0, 0, 1]. The structure of the 4H-$SnSe_2$ polytype (i.e. $P6_3mc$) is composed of two types of chemically equivalents layers alternating each other (ABAB), related one to another by mirror transformation *m* (*x*, *y*, 0), and both characterized by a stacking vector [0, 0, 1] in respect to $P\bar{3}m1$ crystal cell. Such layered structures are well known to favor the existence of stacking faults. The diffraction peaks of pristine $SnSe_2$ and solely Br-doped samples can be indexed to the standard polytype of $SnSe_2$ ($P\bar{3}m1$, PDF 89-3197, Figure S1a-c) with a clear difference in ratio intensities due to the presence of a strong preferential orientation along the [001] direction. Such preferential orientation is taken into account during the Rietveld fit by the March-Dollase function (alignment factor 0.699(1) and 0.671(1) for $SnSe_{1.97}Br_{0.03}$-0% Cu-BHT and -AHT samples respectively) and is due to a platelet crystalline habit of crystallite that is reflected in a small anisotropy in peaks broadening. Upon thermal treatment, the solely Br-doped samples present minimal differences. In contrast, the powder diffraction patterns of $SnSe_{1.97}Br_{0.03}$-3% Cu-BHT and -AHT samples, shown in Figure 2b, present a more complex behavior. As a first observation, the present peaks match with the simulated pattern of $SnSe_2$ in the form of SG $P6_3mc$, another polytype (i.e. 4H-$SnSe_2$) that could be encountered by changing the synthesis temperature in SnS_2 [42,45]. It is inferred that, for the low-temperature hydrothermal synthesis of $SnSe_2$, the addition of Cu plays an important role in the phase

transition from $P\bar{3}m1$ to $P6_3mc$. Indeed, the presence of some spurious peaks on both patterns of Cu added samples may be ascribed to a few percent of sphalerite-derivative Cu-Sn-Se phase (i.e. Cu_2SnSe_3) and Cu_xSe in the Cu-containing samples. The electron probe microscopic analysis (EPMA) quantitative analysis in $SnSe_2$ matrix, shows that still a significative amount (0.65%) of Cu enters into $SnSe_2$ matrix, (Table S4). Note that powder XRD patterns of $SnSe_{1.97}Br_{0.03}$-x% Cu-BHT (x = 2, 4) samples (Figure S1d) also reveal the presence of the 4H-$SnSe_2$ polytype, supporting the importance of Cu in the stabilization of this structure.

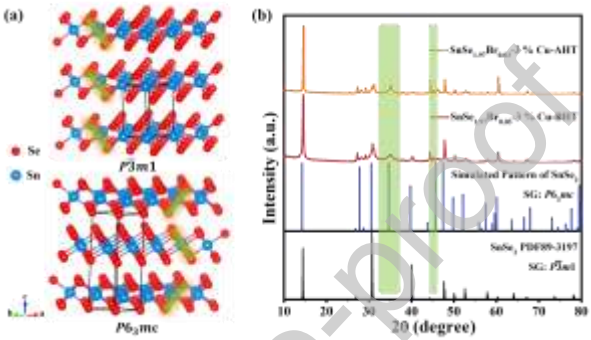

Figure 2. a) The crystal structure models of $SnSe_2$, and b) XRD patterns of $SnSe_{1.97}Br_{0.03}$-3% Cu-BHT/AHT samples.

To gain insight into the difference between the two structures, we investigated the microstructure for $SnSe_{1.97}Br_{0.03}$-x% Cu-BHT/AHT samples (x = 0, 3) by transmission electron microscopy (TEM) and spherical aberration-corrected scanning transmission electron microscopy (Cs-STEM). First, based on the selected area electron diffraction (SAED) patterns obtained from the different samples (Figure 3) and the simulated SAED patterns visualized along [010] zone axis (Figure S2), it can be concluded that the addition of Cu favors a phase transition from $P\bar{3}m1$ to $P6_3mc$ in $SnSe_2$, which is consistent with the powder XRD results. Second, for the $SnSe_{1.97}Br_{0.03}$-BHT and -AHT samples, the SAED patterns are characterized by diffuse streaks along the c axis and typical liner contrast can be seen in the TEM images (Figure 3a and 3b) suggesting the presence of stacking faults. Interestingly, the $SnSe_{1.97}Br_{0.03}$-3% Cu-BHT sample also presents typical liner contrast in the TEM images (Figure 3c) with significant strikes on

its SAED pattern, supporting the presence of stacking faults. On the opposite, for $SnSe_{1.97}Br_{0.03}$-3% Cu-AHT sample, SAED patterns appear quite clean, composed of well-separated peaks (Figure 3d). Finally, after the heat treatment, the stacking faults are retained in the $SnSe_{1.97}Br_{0.03}$ sample (Figure 3b), while they are significantly reduced in the $SnSe_{1.97}Br_{0.03}$-3% Cu sample (Figure 3d). Furthermore, the reduction of stacking fault density facilitated by addition of Cu can be directly observed in the TEM images shown in Figure 3. Both samples are after heat treatment, but the one without Cu shows a plenty of stacking faults while the one with Cu barely shows a significant number of stacking faults.

Now, we need to explain why the addition of Cu can induce a phase transition and the heat treatment has different effects on stacking fault density of $SnSe_{1.97}Br_{0.03}$ and $SnSe_{1.97}Br_{0.03}$-3% Cu samples. The total energy of different $SnSe_2$ samples was calculated by density functional theory (DFT) based on different structure models as listed in Table 1, in which the value of pristine $SnSe_2$ (E_p) with SG $P\bar{3}m1$ was set to be 0 meV. It is found that when Cu is added into $SnSe_2$, the total energy (E_{Cu}) of the structure with SG $P\bar{3}m1$ has higher energy than that with SG $P6_3mc$, which implies that the latter case is more stable. Namely, the addition of Cu facilitates the phase transition from SG $P\bar{3}m1$ to SG $P6_3mc$. In addition, the formation energy of stacking faults ΔE of $SnSe_{1.97}Br_{0.03}$-3% Cu sample (173 meV) with SG $P6_3mc$ is much higher than that of the $SnSe_{1.97}Br_{0.03}$ sample (75 meV) with SG $P\bar{3}m1$. These results are in agreement with the experimental TEM observation showing that the stacking faults in Cu-added samples with $P6_3mc$ structure are more easily to be eliminated by heat treatment than those with $P\bar{3}m1$ structure.

Table 1. The calculated E_p (the total energy of pristine $SnSe_2$), E_{sf} (the total energy of $SnSe_2$ with stacking faults), E_{Cu} (the total energy of $SnSe_2$ with Cu), and ΔE (= E_{sf} - E_p, the formation energy of stacking faults) of $SnSe_2$ in different configurations.

Space group	E_p (meV)	E_{sf} (meV)	E_{Cu} (meV)	ΔE (meV)
$P\bar{3}m1$	0	75	23	75
$P6_3mc$	22	195	8	173

The energy-dispersive X-ray spectroscopy (EDX) mapping of $SnSe_{1.97}Br_{0.03}$-3% Cu-AHT sample (Figure S3) reveals that all elements are uniformly distributed in the matrix. High-angle annular-dark field (HADDF)-STEM images of the $SnSe_{1.97}Br_{0.03}$-AHT and $SnSe_{1.97}Br_{0.03}$-3% Cu-AHT samples are presented in the inset of Figure 3b,d, respectively. From the insets, the triatomic (i.e. Se-Sn-Se) layers of $SnSe_2$ and the vdW gaps between them can be clearly observed. As the higher atomic number indicates the stronger signal for HAADF-STEM image, Sn^{50} atoms should be placed in larger and brighter spots in the central atomic layer, while dimmer spots in the outer atomic layers should be assigned to Se^{34} or Br^{35} atoms. Several dots with weak signals are traced in the vdW gaps, which should be the insertion of Cu^{29} atoms (Figure S3b) [30]. Notably, for the $SnSe_{1.97}Br_{0.03}$-3% Cu-AHT sample, two adjacent triatomic layers are aligned in the opposite directions for each other and stacked through vdW interactions to form the $P6_3mc$ structure. However, for the $SnSe_{1.97}Br_{0.03}$-AHT sample, the arrangement of each layer is the same, as the common $P\bar{3}m1$ structure. These interesting findings inspired us to explore the feasibility of tuning the density of stacking faults through phase manipulation to optimize the TE performance of $SnSe_2$.

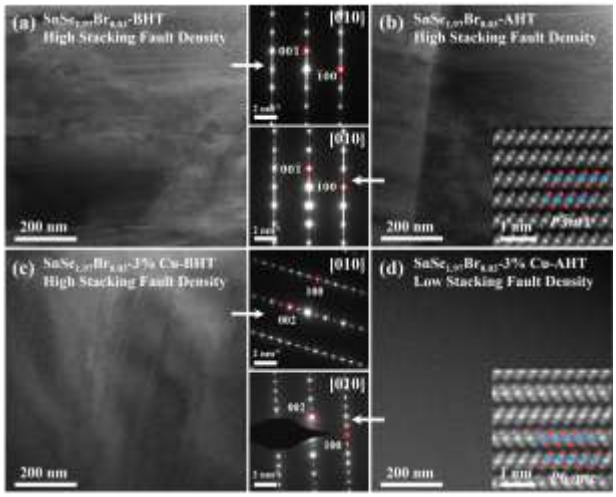

Figure 3. TEM images and corresponding SAED patterns for a) $SnSe_{1.97}Br_{0.03}$-BHT sample, b) $SnSe_{1.97}Br_{0.03}$-AHT sample, c) $SnSe_{1.97}Br_{0.03}$-3% Cu-BHT sample, and d) $SnSe_{1.97}Br_{0.03}$-3% Cu-AHT sample (inset: HAADF-STEM images).

3.2. Electrical Transport Properties and Origin of Enhanced Carrier Mobility

Referring to our previous study on $SnSe_2$ [37], the optimal Br doping concentration is 3 at.%. Accordingly, Cu was introduced into the samples with the nominal composition of $SnSe_{1.97}Br_{0.03}$ to regulate its structure. Electrical and thermal transport data for all samples in this study were collected along the hot-pressing orientation because of the better TE performance along the *c*-axis reported in literature [24]. The temperature-dependent σ is plotted in Figure 4a for bulk $SnSe_2$ and $SnSe_{1.97}Br_{0.03}$-x% Cu-BHT (x = 0, 2, 3, 4) samples. The σ of the pristine $SnSe_2$ is very low due to the low carrier concentration (n), which is dramatically boosted by Br doping. The $SnSe_{1.97}Br_{0.03}$ sample shows a degenerate semiconductor behavior where σ decreases with increasing temperature. This situation can be ameliorated by Cu addition, since more charge carriers are excited for Cu-added samples as the temperature increases [30]. Consequently, σ increases in $SnSe_{1.97}Br_{0.03}$-x% Cu (x = 2, 3, 4) samples from 523 K as shown in Figure 4a, and reached values are nearly five times of that for Br-doped sample at 773 K. In Figure 4b, the negative S values for all samples indicate n-type conducting behavior, and the variation in $|S|$ can be attributed to the difference in n

values [37]. The conduction band minimum (CBM) moves from **L** to **M** point after the phase transition, indicating the band degeneracy of 3 for both phases as shown in Figure 4c,d. Besides, in spite of the diminished band gap, the band dispersion curve near the CBM is almost unchanged, which indicates that the phase transition can hardly affect the intrinsic electrical properties of $SnSe_2$ [15,26]. The Pisarenko curve shows the experimental values of $|S|$ fall on the curve with an effective mass (m^*) of ~1.8 m_e, where the m_e is the mass of free electron, indicating that the addition of Cu has negligible influence on the band dispersion of the conduction band edge (Figure S4).

The temperature-dependent κ and κ_l of all BHT-samples are plotted in Figure S4b,c, respectively, and the inset is κ_e. The details for estimation of κ_e are given in the supporting materials (SM). The decrease in κ with increasing temperature for all samples suggests a common phonon-phonon scattering-dominated thermal transport behavior. Although κ_e values increase resulting from the enlarged σ, the electronic contribution to the total heat transport is still negligibly small. Therefore, κ_l is dominant in total κ. For both the Br-doped sample and the Cu-Br co-doped samples, the κ_l values do not vary significantly, which indicates that the Cu-induced structural phase transition and microstructural defects have a negligible effect on κ_l. The power factors ($PF = S^2\sigma$) for bulk $SnSe_2$ and BHT samples are displayed in Figure 4e. It is found that an enhanced PF of 6.1 μW cm^{-1} K^{-2} at 773 K is obtained in the $SnSe_{1.97}Br_{0.03}$-3% Cu-BHT sample, which would be attributed to the enlarged n (Figure 4f) triggered by Cu addition compared to that of Br-doped sample in Ref. 43. Based on the first-principles calculation results in our previous work [37], the obtained n approaches the optimal value. On that account, further improvement of the power factor should rely on increasing the mobility of polycrystalline samples, which can be achieved by the heat treatment.

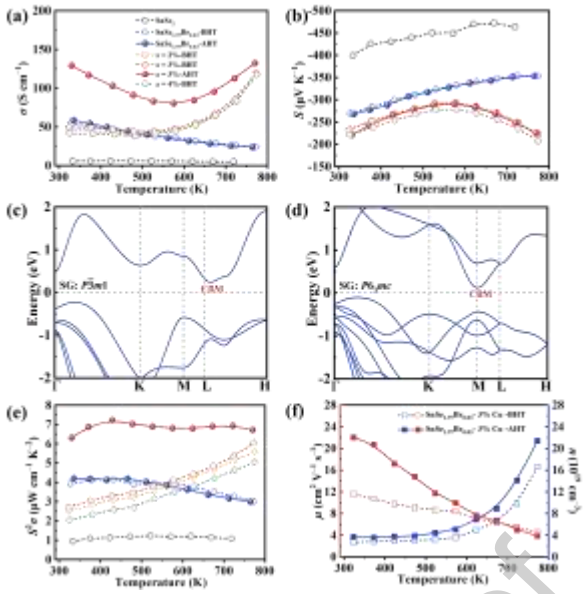

Figure 4. Temperature-dependent a) σ, b) S, and e) $S^2\sigma$ for bulk $SnSe_2$, $SnSe_{1.97}Br_{0.03}$-x% Cu-BHT (x = 0, 2, 3, and 4) and $SnSe_{1.97}Br_{0.03}$-x% Cu-AHT (x = 0, 3) samples. c,d) The electronic band structures of $SnSe_2$ with SG $P\bar{3}m1$ and SG $P6_3mc$, respectively. f) Temperature-dependent μ and n of $SnSe_{1.97}Br_{0.03}$-3% Cu-BHT/AHT samples.

The temperature-dependent σ and S of $SnSe_{1.97}Br_{0.03}$-x% Cu-AHT (x = 0, 3) samples are presented in Figure 4a,b, respectively. The σ and $|S|$ values of the solely Br-doped samples are not affected by the heat treatment. The variation in σ and S of $SnSe_{1.97}Br_{0.03}$-3% Cu-AHT sample over the entire temperature range is consistent with that of $SnSe_{1.97}Br_{0.03}$-3% Cu-BHT sample. Unexpectedly, the σ values of Br-doped samples with addition of Cu are significantly improved from 51 S cm^{-1} to 129 S cm^{-1} at 323 K by heat treatment, while $|S|$ values are basically unchanged owing to the similar n as shown in Figure 4f. This implies that the heat treatment can effectively improve the carrier mobility of Cu-Br co-doped samples. It is worth mentioning that the Cu-introduced $SnSe_{1.97}Br_{0.03}$ samples show strong temperature dependent carrier concentration, which can offer us an opportunity to dynamically regulate the carrier density close to the optimized value especially in the high-temperature region and thus is beneficial to obtaining high power factors and also high average ZT [46,47]. As shown in Figure 4f, the carrier concentration in Cu-introduced $SnSe_{1.97}Br_{0.03}$ samples

continuously increases from 323 K to 773 K, in which the dynamic Cu intercalates into the van der Waals gap in $SnSe_2$ as temperature rises. This is completely different from the static doping by Br [48]. Consequently, high *PF* values close to 6.3 and 6.7 μW cm^{-1} K^{-2} are obtained at 323 K and 773 K for the $SnSe_{1.97}Br_{0.03}$-3% Cu-AHT sample, respectively (Figure 4e). It is worth mentioning that $SnSe_{1.97}Br_{0.03}$-3% Cu-AHT sample has the highest average power factor (PF_{ave}) of 6.9 μW cm^{-1} K^{-2} along out-of-plane direction in the entire temperature range among *n*-type $SnSe_2$-based TE materials, which is even superior to that of *n*-type polycrystalline SnSe, as shown in Figure S5 [23,25,29,30,36,49]. In order to probe this favorable "decoupling" phenomenon in the $SnSe_{1.97}Br_{0.03}$-3% Cu-AHT sample, the μ values of these samples before and after a heat treatment were calculated by the formula $\mu = \sigma/ne$ and the results are displayed in Figure 4f. Strikingly, with similar *n* before and after the heat treatment, the μ of $SnSe_{1.97}Br_{0.03}$-3% Cu samples is improved from 11 cm^2 V^{-1} s^{-1} to 22 cm^2 V^{-1} s^{-1} at 323 K after the heating, which is highly beneficial to improve the PF_{ave}. To account for the greatly increased μ, we consider both acoustic phonon (ac) and grain boundary (b) scattering processes for carriers. Here, the charge carrier transport is analyzed using Matthiessen's rule [50]:

$$\mu^{-1} = \mu_b^{-1} + \mu_{ac}^{-1} \quad (1)$$

$$\mu_b(T) = AT^{-\frac{1}{2}}e^{-\frac{B}{T}} \quad (2)$$

$$\mu_{ac}(T) = C\left(\frac{T}{300}\right)^{-\frac{3}{2}} \quad (3)$$

where A and B represent parameters positively related to grain size and energy barrier height for crossing the grain boundaries, respectively. C stands for room temperature μ only considering phonon scattering. By fitting these equations with experimental μ data, it is found that the A value is enlarged from 192 to 424 for $SnSe_{1.97}Br_{0.03}$-3% Cu sample after the heat treatment. Therefore, the significantly increased mobilities in the temperature region of 323 K-523 K can be attributed to a reduction of the stacking fault density in $SnSe_{1.97}Br_{0.03}$-3% Cu-AHT sample after the heat treatment possibly coupled to a larger grain size. The relationship between the density of stacking faults and grain

size will be discussed in the next section. Above 523 K, the mobilities of the samples before and after heat treatment are similar, where the electron-phonon interaction dominates the carrier scattering.

To further elucidate the relationship between microstructure and enhanced μ, HAADF-STEM images of $SnSe_{1.97}Br_{0.03}$-3% Cu-BHT (Figure 5a) and $SnSe_{1.97}Br_{0.03}$-3% Cu-AHT (Figure 5c) samples were further analyzed. Through image processing, the stacking (or displacement) maps are obtained and presented in Figure 5b,d. The image processing can be found in the SM (the section of HAADF image processing methods and Figure S6). As depicted in Figure 5d, the Sn layers (which represent the stacking sequence of Se-Sn-Se layers) show periodic stacking sequence with alternatively blue and red layers, which is well consistent with the structure of the 4H-$SnSe_2$ polytype ($P6_3mc$). In contrast, the stacking sequence seems to be irregular in Figure 5b, suggesting the existence of stacking faults. The stacking sequence maps of whole images of Figure 5a,c are shown in Figure S6e,h, which further stress that the density of stacking faults of Cu-introduced $SnSe_{1.97}Br_{0.03}$ sample is significantly reduced after the heat treatment, which coincides with the above discussion (Figure 3). It is worth noting that this image process is valuable for the identification of stacking faults based on the atomic-resolved HAADF images. Commonly, the stacking faults should be identified carefully on the HAADF (or HRTEM) images, as seen in the middle panel of Figure 5, which is usually time-consuming and hard to distinguish. However, using this image processing, we can map the stacking sequence of the images quickly, accurately, and observably, which is beneficial to the rapid identification of stacking faults. Thus, this method is expected to be used in other materials, particularly in layered structures.

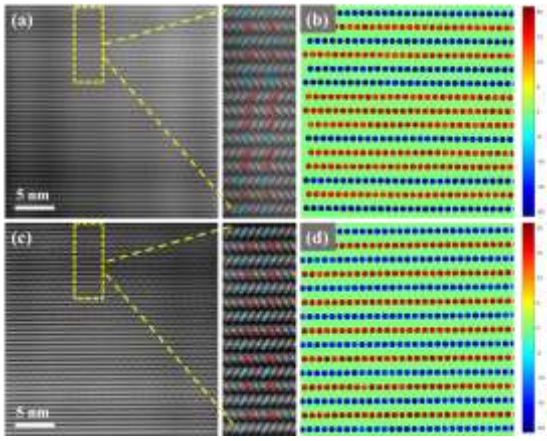

Figure 5. High-magnification atomic-resolution HAADF-STEM images and corresponding simulation diagrams for $SnSe_{1.97}Br_{0.03}$-3% Cu samples: a,b) BHT sample and c,d) AHT sample.

Considering that thermal energy favors grain growth and reduces the stacking faults density, an increase of μ in $SnSe_2$ sample after heat treatment is expected [51]. The SEM images presented in Figure S7, show a clear increase in thickness along the stacking direction of $SnSe_2$ layers. Both the $SnSe_{1.97}Br_{0.03}$ (Figure S7a) and $SnSe_{1.97}Br_{0.03}$-3% Cu (Figure S7c) samples before the heat treatment exhibit a distinct layered feature, which is responsible for the anisotropic thermal and electrical transport properties. In detail, the bulk samples consist of layers arranged almost in the same direction. The thickness of layers for the sample without Cu addition remains at the same order of magnitude after the heat treatment (Figure S7b). On the contrary, as shown in Figure S7d, the thickness of layers for the $SnSe_{1.97}Br_{0.03}$-3% Cu sample seems to be increased to several micrometers after the heat treatment, suggesting that the grains further grow with the 4H-$SnSe_2$ polytype stabilized by Cu with possibly a less inhibition from stacking faults during the heat treatment [52]. Interestingly, some pores emerge as the grains grow (Figure S7d,e), and the thermogravimetric analysis (TGA) shows that there is no thermal decomposition from 300 to 773 K (Figure S7f). So, the reduction in relative density is mainly related to volume change during the heat treatment rather than weight loss. It is worth mentioning that this pore structure can not only contribute to the further reduction in thermal conductivity, but also provide better

portability [53].

3.3. Thermal Conductivity and Figure of Merit for AHT Samples

Figure 6a presents the temperature-dependent κ of $SnSe_{1.97}Br_{0.03}$-x% Cu samples (x = 0, 3) before and after the heat treatment. Obviously, the κ of all samples decreases with increasing temperature as expected. The κ of $SnSe_{1.97}Br_{0.03}$-3% Cu-AHT sample declines from 1.2 W m^{-1} K^{-1} at 323 K to 0.45 W m^{-1} K^{-1} at 773 K, which is 33% and 35% lower than that of $SnSe_{1.97}Br_{0.03}$-3% Cu-BHT sample, respectively. In contrast, the κ of the $SnSe_{1.97}Br_{0.03}$ sample is unchanged by the heat treatment. Although the number of stacking faults and grain boundaries are reduced, the κ of the $SnSe_{1.97}Br_{0.03}$-3% Cu-AHT sample can be significantly suppressed by the formation of pores. As shown in Figure 6b, the decrease in κ of the porous $SnSe_{1.97}Br_{0.03}$-3% Cu-AHT sample mainly stems from the greatly suppressed κ_l, and its calculation details are provided in the SM. An ultra-low κ_l of 0.29 W m^{-1} K^{-1} has been achieved in porous $SnSe_{1.97}Br_{0.03}$-3% Cu-AHT sample, which is closed to the predicted minimum lattice thermal conductivity given by the Cahill-Pohl model. Besides, the elevated μ leads to a larger κ_e of $SnSe_{1.97}Br_{0.03}$-3% Cu-AHT sample than those of the others, manifested markedly in the inset of Figure 6b.

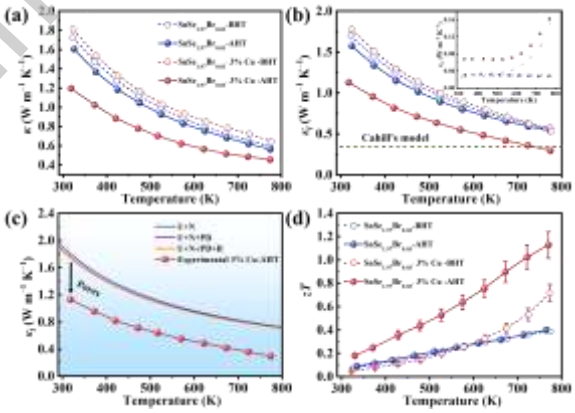

Figure 6. a) κ and b) κ_l (inset: κ_e) with respect to temperature for $SnSe_{1.97}Br_{0.03}$-x% Cu-BHT/AHT samples (x = 0, 3), c) the experimental and the predicted EMT-corrected κ_l based on the Debye-Callaway model, which considers the Umklapp process (U), Normal process (N), point defects (PD), and grain boundaries (B), d) temperature-

dependent zT of $SnSe_{1.97}Br_{0.03}$-x% Cu-BHT/AHT samples (x = 0, 3).

To elucidate the scattering mechanism of phonons, the lattice thermal conductivity was analyzed considering different scattering sources. First, the lattice thermal conductivity of theoretically fully dense $SnSe_{1.97}Br_{0.03}$-3% Cu-AHT sample ($\kappa_{l,f}$) is acquired by Equation (4-5) based on the effective medium theory (EMT) [53,54]:

$$\kappa_{l,f} = \frac{\kappa_{l,p}}{\left(1 - \frac{3\varepsilon}{2}\right)} \quad (4)$$

$$\varepsilon = 1 - \frac{\rho}{\rho_0} \quad (5)$$

where $\kappa_{l,p}$, ε and ρ/ρ_0 refer to the lattice thermal conductivity, porosity and relative density for porous materials, respectively. Second, $\kappa_{l,f}$ was calculated using the Debye-Callaway model considering Umklapp (U) and Normal (N) processes, point defects (PD), and grain boundaries (B), and the details are provided in the SM. It can be seen from Figure 6c that the U+N process is the main scattering mechanism, while point defects and grain boundaries have almost negligible effect on the lattice thermal conductivity of these samples. This is mainly because the low lattice thermal conductivity of $SnSe_2$ originates from the inherent small phonon group velocity and strong lattice anharmonicity [26,55]. Furthermore, the grain size dependent κ_l was calculated by DFT and depicted in Figure S8a. The results show that κ_l can only be reduced when minimizing the grain size to below 5 nm, which is consistent with the fitting results of the Debye-Callaway model. By analyzing the scattering mechanism of phonons, it is further demonstrated that the ultra-low κ_l observed in the experiment benefits from porosity, which can be seen clearly in Figure S7d. Consequently, the κ_l of porous $SnSe_{1.97}Br_{0.03}$-3% Cu-AHT sample drops by 37% and 46% compared with the dense $SnSe_{1.97}Br_{0.03}$-3% Cu-BHT sample at 323 K and 773 K, respectively. Although the pores lead to noticeable reduction in lattice thermal conductivity, the electron mobility of porous $SnSe_{1.97}Br_{0.03}$-3% Cu-AHT sample is unexpectedly well maintained (Figure 4f), possibly benefiting from the large grain size and good crystallinity. In general, there are two types of pores in the materials: pores exist in "in-grain" and "out-

grain" region. In the case of $SnSe_{1.97}Br_{0.03}$-3% Cu-AHT sample, the pores exist in out-grain region (Figure S9a-b), similar to those reported by Wu et al [53]. Their results also show a reduced thermal conductivity but the electrical performance has not been deteriorated, indicating that the introduction of pores existing in out-grain region may also be beneficial to improve TE performance. It may be questioned that these grains are not well packed due to the pores existing in out-grain region and the mechanical properties may be worsened. Additional SEM analysis was performed by collecting the images of the FIB-cut specimen from the $SnSe_{1.97}Br_{0.03}$-3% Cu-AHT sample. The results show that the sample is well-packed, indicating that mechanical property of the sample after heat treatment is not worsened as suggested by the Vickers hardness measurement (shown in Table S5). As a result, a greatly improved peak zT of 1.13 is obtained at 773 K in $SnSe_{1.97}Br_{0.03}$-3% Cu-AHT sample (Figure 6d), which is more than 700% enhancement compared to pristine $SnSe_2$ sample (Figure S4d). It is worth noting that, as shown in Figure 1b, the peak zT is the record-high value for $SnSe_2$-based materials. Figure S8b-f and Figure S9 present good reproducibility and stability, which were obtained from the reversible measurements of $SnSe_{1.97}Br_{0.03}$-3% Cu-AHT sample upon thermal cycling. Besides, the thermoelectric properties of $SnSe_{1.97}Br_{0.03}$-x% Cu-AHT samples (x = 2, 4) along the direction parallel to hot press and $SnSe_{1.97}Br_{0.03}$-x% Cu-BHT/AHT samples (x = 0, 3) along the perpendicular direction to hot press have been plotted in Figure S11 and S12, respectively. More importantly, benefiting by the greatly improved μ especially near room temperature, a record-high ZT_{ave} of 0.62 is achieved in $SnSe_{1.97}Br_{0.03}$-3% Cu-AHT sample from 323 K to 773 K, exceeding all the other state-of-the-art n-type polycrystalline layered compounds working in intermediate-to-high temperature region (Figure 1c).

4. Conclusion

In conclusion, stacking faults are most likely not beneficial for layered TE compounds with intrinsically low lattice thermal conductivity as demonstrated in the case of $SnSe_2$. A crystal structure modification from the 2H-$SnSe_2$ polytype (SG $P\bar{3}m1$) to the 4H-$SnSe_2$ polytype (SG $P6_3mc$) is triggered by introducing Cu into $SnSe_2$ matrix.

A low stacking fault density is found in $SnSe_{1.97}Br_{0.03}$-3% Cu sample holding $P6_3mc$ structure, in which the formation energy of stacking faults is high compared to $P\bar{3}m1$ structure. After heat treatment, the reduced stacking fault density and enlarged grain size result in a significantly improved μ and thereby a remarkable enhancement of PF. Combined with the ultralow κ_l in $SnSe_{1.97}Br_{0.03}$-3% Cu-AHT sample, a record-high peak zT and ZT_{ave} are attained. These findings provide a new strategy to synergistically optimize the electron and phonon transport towards excellent TE performance for layered compounds through phase-dependent microstructure modification.

Declaration of Competing Interest

The authors declare that they have no known competing financial interests or personal relationships that could have appeared to influence the work reported in this paper.

Acknowledgments

This work was financially supported by the National Natural Science Foundation of China (Grant Nos. 12274044, 52125103, and 52071041). This work was also financially supported in part by the Chongqing Entrepreneurship and Innovation Program for the Returned Overseas Chinese Scholars (No. cx2022047) and the Instrument Function Developing Project of Chongqing University (No. gnkf2022003). The authors would like to thank the Analytical and Testing Center of Chongqing University for the assistance with the sample characterization.

Supplementary materials

Supplementary material associated with this article can be found in the online version, at.

References

[1] P. Lemoine, G. Guelou, B. Raveau, E. Guilmeau, Crystal structure classification of copper-based sulfides as a tool for the design of inorganic functional materials,

Angew. Chem. Int. Ed. 61 (2022) e202108686.

[2] X. Lu, Q. Zhang, J. Liao, H. Chen, Y. Fan, J. Xing, S. Gu, J. Huang, J. Ma, J. Wang, L. Wang, W. Jiang, High-efficiency thermoelectric power generation enabled by homogeneous incorporation of MXene in $(Bi,Sb)_2Te_3$ matrix, Adv. Energy Mater. 10 (2019) 1902986.

[3] N. Jia, X. Y. Tan, J. W. Xu, Q. Y. Yan, M. G. Kanatzidis, Achieving enhanced thermoelectric performance in multiphase materials, Acc. Mater. Res. 3 (2022) 237-246.

[4] X. L. Shi, J. Zou, Z. G. Chen, Advanced thermoelectric design: from materials and structures to devices, Chem. Rev. 120 (2020) 7399-7515.

[5] Z. H. Liu, W. H. Gao, F. K. Guo, W. Cai, Q. Zhang, J. H. Sui, Challenges for thermoelectric power generation: from a material perspective, Mater. Lab 1 (2022) 220003.

[6] Y. Xiao, L. Xu, T. Hong, H. Shi, S. Wang, X. Gao, X. Ding, J. Sun, L. D. Zhao, Ultrahigh carrier mobility contributes to remarkably enhanced thermoelectric performance in n-type PbSe, Energy Environ. Sci. 15 (2022), 346-355.

[7] Y. Zheng, T. J. Slade, L. Hu, X. Y. Tan, Y. Luo, Z. Z. Luo, J. Xu, Q. Yan, M. G. Kanatzidis, Defect engineering in thermoelectric materials: what have we learned? Chem. Soc. Rev. 50 (2021) 9022-9054.

[8] Z. Chen, X. Zhang, Y. Pei, Manipulation of phonon transport in thermoelectrics, Adv. Mater. 30 (2018) e1705617.

[9] B. C. Qin, L. D. Zhao, Carriers: the less, the faster, Mater. Lab 1 (2022) 220004.

[10] G. Han, S. R. Popuri, H. F. Greer, L. F. Llin, J. W. G. Bos, W. Z. Zhou, D. J. Paul, H. Menard, A. R. Knox, A. Montecucco, J. Siviter, E. A. Man, W. G. Li, M. C. Paul, M. Gao, T. Sweet, R. Freer, F. Azough, H. Baig, T. K. Mallick, D. H. Gregory, Chlorine-enabled electron doping in solution-synthesized SnSe thermoelectric nanomaterials, Adv. Energy Mater. 7 (2017) 1602328.

[11] C. Wan, Y. Wang, W. Norimatsu, M. Kusunoki, K. Koumoto, Nanoscale stacking faults induced low thermal conductivity in thermoelectric layered metal sulfides, Appl. Phys. Lett. 100 (2012) 101913.

[12] Q. Sun, M. Li, X. L. Shi, S. D. Xu, W. D. Liu, M. Hong, W. Y. Lyu, Y. Yin, M. Dargusch, J. Zou, Z. G. Chen, Versatile vanadium doping induces high thermoelectric performance in GeTe via band alignment and structural modulation, Adv. Energy Mater. 11 (2021) 2100544.

[13] M. Hong, Z. G. Chen, L. Yang, Z. M. Liao, Y. C. Zou, Y. H. Chen, S. Matsumura, J. Zou, Achieving zT > 2 in p-Type $AgSbTe_{2-x}Se_x$ alloys via exploring the extra light valence band and introducing dense stacking faults, Adv. Energy Mater. 8 (2017) 1702333.

[14] J. M. Ziman, Electrons and phonons, Clrendon Press: Oxford, 1960.

[15] S. S Das, M. G. Rosul, M. Zebarjadi, Optimization of the thermoelectric properties of $SnSe_2$ using first-principles calculations, J. Phys. Chem. C 127 (2023) 6916-6924.

[16] G. Zhang, Y. W. Zhang, Thermoelectric properties of two-dimensional transition metal dichalcogenides, J. Mater. Chem. C 5 (2017) 7684-7698.

[17] Y. Luo, Z. Ma, S. Hao, S. Cai, Z. Z. Luo, C. Wolverton, V. P. Dravid, J. Yang, Q. Yan, M. G. Kanatzidis, Thermoelectric performance of the 2D $Bi_2Si_2Te_6$ semiconductor, J. Am. Chem. Soc. 144 (2022) 1445-1454.

[18] T. Deng, Z. Q. Gao, P. F. Qiu, T. R. Wei, J. Xiao, G. S. Wang, L. D. Chen, and X. Shi, Plastic/ductile bulk 2D van der waals single-crystalline $SnSe_2$ for flexible thermoelectrics, Adv. Sci. 9 (2022) 2203436.

[19] Z. G. Chen, X. Shi, L. D. Zhao, J. Zou, High-performance SnSe thermoelectric materials: progress and future challenge, Prog. Mater Sci. 97 (2018) 283-346.

[20] Y. Zhou, L. D. Zhao, Promising thermoelectric bulk materials with 2D structures, Adv. Mater. 29 (2017) 1702676.

[21] M. Martín-González, O. Caballero-Calero, P. Díaz-Chao, Nanoengineering thermoelectrics for 21st century: energy harvesting and other trends in the field, Renewable Sustainable Energy Rev. 24 (2013) 288-305.

[22] L. D. Zhao, S. H. Lo, Y. Zhang, H. Sun, G. Tan, C. Uher, C. Wolverton, V. P. Dravid, M. G. Kanatzidis, Ultralow Thermal conductivity and high thermoelectric figure of merit in SnSe crystals, Nature 508 (2014) 373-377.

[23] S. Li, Y. Wang, C. Chen, X. Li, W. Xue, X. Wang, Z. Zhang, F. Cao, J. Sui, X. Liu, Q. Zhang, Heavy doping by bromine to improve the thermoelectric properties of n-type polycrystalline SnSe, Adv. Sci. 5 (2018) 1800598.

[24] P. Xu, T. Fu, J. Xin, Y. Liu, P. Ying, X. Zhao, H. Pan, T. Zhu, Anisotropic thermoelectric properties of layered compound $SnSe_2$, Sci. Bull. 62 (2017) 1663-1668.

[25] Y. Luo, Y. Zheng, Z. Luo, S. Hao, C. Du, Q. Liang, Z. Li, K. A. Khor, K. Hippalgaonkar, J. Xu, Q. Yan, C. Wolverton, M. G. Kanatzidis, n-Type $SnSe_2$ oriented-nanoplate-based pellets for high thermoelectric performance, Adv. Energy Mater. 8 (2018) 1702167.

[26] Y. Wu, W. Li, A. Faghaninia, Z. Chen, J. Li, X. Zhang, B. Gao, S. Lin, B. Zhou, A. Jain, Y. Pei, Promising thermoelectric performance in van der waals layered $SnSe_2$, Mater. Today Phys. 3 (2017) 127-136.

[27] Y. Zhang, Y. Liu, K. H. Lim, C. Xing, M. Li, T. Zhang, P. Tang, J. Arbiol, J. Llorca, K. M. Ng, M. Ibanez, P. Guardia, M. Prato, D. Cadavid, A. Cabot, Tin diselenide molecular precursor for solution-processable thermoelectric materials, Angew. Chem. Int. Ed. 57 (2018) 17063-17068.

[28] S. Wu, H. Yang, Z. Wu, C. Liu, L. Miao, J. Gao, X. Wang, X. Wang, C. Shen, J. G. Noudem, J. Wang, Enhancement of thermoelectric performance of layered $SnSe_2$ by synergistic modulation of carrier concentration and suppression of lattice thermal conductivity, ACS Appl. Energy Mater. 2 (2019) 8481-8490.

[29] C. Liu, Z. Huang, D. Wang, X. Wang, L. Miao, X. Wang, S. Wu, N. Toyama, T. Asaka, J. Chen, E. Nishibori, L. D. Zhao, Dynamic Ag^+-intercalation with $AgSnSe_2$ nano-precipitates in Cl-doped polycrystalline $SnSe_2$ toward ultra-high thermoelectric performance, J. Mater. Chem. A 7 (2019) 9761-9772.

[30] C. Zhou, Y. Yu, X. Zhang, Y. Cheng, J. Xu, Y. K. Lee, B. Yoo, O. Cojocaru-Mirédin, G. Liu, S. P. Cho, M. Wuttig, T. Hyeon, I. Chung, Cu intercalation and Br doping to thermoelectric $SnSe_2$ lead to ultrahigh electron mobility and temperature-independent power factor, Adv. Funct. Mater. 30 (2019) 1908405.

[31] Y. Gu, K. Song, X. Hu, C. Chen, L. Pan, C. Lu, X. Shen, K. Koumoto, Y. Wang,

Realization of an ultrahigh power factor and enhanced thermoelectric performance in TiS_2 via microstructural texture engineering, ACS Appl. Mater. Inter. 12 (2020) 41687-41695.

[32] K. Jin, J. Tiwari, T. Feng, Y. Lou, B. Xu, Realizing high thermoelectric performance in eco-friendly Bi_2S_3 with nanopores and Cl-doping through shape-controlled nano precursors, Nano Energy 100 (2022) 107478.

[33] L. Pan, L. Zhao, X. Zhang, C. Chen, P. Yao, C. Jiang, X. Shen, Y. Lyu, C. Lu, L. D. Zhao, Y. Wang, Significant optimization of electron-phonon transport of n-type Bi_2O_2Se by mechanical manipulation of Se vacancies via shear exfoliation, ACS Appl. Mater. Interfaces 11 (2019) 21603-21609.

[34] M. Li, Y. Zhang, T. Zhang, Y. Zuo, K. Xiao, J. Arbiol, J. Llorca, Y. Liu, A. Cabot, Enhanced thermoelectric performance of n-Type Bi_2Se_3 nanosheets through Sn doping, Nanomaterials 11 (2021) 1827.

[35] S. H. He, P. F. Liu, Z. X. Lin, G. Q. Wang, L. Chen, Z. X. Wang, L. M. Wu, The roles of Yb-substitution on thermoelectric properties of $In_{4-x}Yb_xSe_3$, Acta Mater. 101 (2015) 16-21.

[36] S. Chandra, U. Bhat, P. Dutta, A. Bhardwaj, R. Datta, K. Biswas, Modular nanostructures facilitate low thermal conductivity and ultra-high thermoelectric performance in n-Type SnSe, Adv. Mater. 34 (2022) e2203725.

[37] Y. Wei, Z. Zhou, J. Liu, B. Zhang, G. Wang, G. Han, G. Wang, X. Zhou, X. Lu, MXene as charge reservoir promotes the thermoelectric performance of layered metal selenide $SnSe_2$, Acta Mater. 241 (2022) 118369.

[38] J. Rodriguez-Carvajal, Recent advances in magnetic structure determination by neutron powder diffraction, Physica B Condens 192 (1993) 55-69.

[39] T. Roisnel, J. Rodriguez-Carvajal, WinPLOTR, a graphic tool for powder diffraction, Mater. Sci. Forum 378-381 (2001) 118-123.

[40] Z. Tong, S. Li, X. Ruan, H. Bao, Comprehensive first-principles analysis of phonon thermal conductivity and electron-phonon coupling in different metals, Phys. Rev. B 100 (2019) 144306.

[41] Z. Zhou, X. Yang, H. Fu, R. Wang, X. Lu, G. Wang, X. Zhou, Anomalous thermal transport driven by electron–phonon coupling in 2D semiconductor h-BP, Adv. Funct. Mater. 32 (2022) 2206974.

[42] S. Zhan, L. Zheng, Y. Xiao, L. D. Zhao, Phonon and carrier transport properties in low-cost and environmentally friendly SnS_2: a promising thermoelectric material, Chem. Mater. 32 (2020) 10348-10356.

[43] S. Acharya, O. N. Srivastava, Occurrence of polytypism in $SnSe_2$, J. Cryst. Growth 55 (1981) 395-397.

[44] B. Patosz, Refinement of SnS_2 polytypes 2H, 4H and 18R, Acta Cryst. B46 (1990) 449-455.

[45] J. C. Mikkelsen, Polytype characterization of SnS_2 crstals grown from Sn-rich melts, J. Cryst. Growth 49 (1980) 253-260.

[46] L. You, Y. F. Liu, X. Li, P. F. Nan, B. H. Ge, Y. Jiang, P. F. Luo, S. S. Pan, Y. Z. Pei, W. Q. Zhang, G. J. Snyder, J. Yang, J. Y. Zhang, J. Luo, Boosting the thermoelectric performance of PbSe through dynamic doping and hierarchical phonon scattering, Energy Environ. Sci. 11 (2018) 1848.

[47] H. Xie, Y. Liu, Y. Zhang, S. Hao, Z. Li, M. Cheng, S. Cai, G. J. Snyder, C. Wolverton, C. Uher, V. P. Dravid, M. G. Kanatzidis, High thermoelectric performance in chalcopyrite $Cu_{1-x}Ag_xGaTe_2$-ZnTe: nontrivial band structure and dynamic doping effect, J. Am. Chem. Soc. 144 (2022) 9113-9125.

[48] A. T. Pham, T. H. Vu, Q. V. Nguyen, M. T. Vu, J. H. Park, S. D. Park, S. Cho, Br-doped n-type $SnSe_2$: single-crystal growth and thermoelectric properties, ACS Appl.Energy Mater. 4 (2021) 2908-2913.

[49] S. Li, F. H. Zhang, C. Chen, X. F. Lia, F. Cao, J. H. Sui, X. J. Liu, Z. F. Ren, Q. Zhang, Enhanced thermoelectric performance in polycrystalline n-type Pr-doped SnSe by hot forging, Acta Mater. 190 (2020) 1-7.

[50] T. R. Wei, G. Tan, X. Zhang, C. F. Wu, J. F. Li, V. P. Dravid, G. J. Snyder, M. G. Kanatzidis, Distinct impact of alkali-ion doping on electrical transport properties of thermoelectric p-type polycrystalline SnSe, J. Am. Chem. Soc. 138 (2016) 8875-82.

[51] L. Xie, Y. Chen, R. Liu, E. Song, T. Xing, T. Deng, Q. Song, J. Liu, R. Zheng, X. Gao, S. Bai, L. Chen, Stacking faults modulation for scattering optimization in GeTe-based thermoelectric materials, Nano Energy 68 (2020) 104347.

[52] H. Stange, S. Brunken, D. Greiner, M. D. Heinemann, D. A. Barragan Yani, L. A. Wägele, C. Li, E. Simsek Sanli, M. Kahnt, S. S. Schmidt, J. P. Bäcker, C. A. Kaufmann, M. Klaus, R. Scheer, C. Genzel, R. Mainz, Stacking fault reduction during annealing in Cu-poor $CuInSe_2$ thin film solar cell absorbers analyzed by in situ XRD and grain growth modeling, J. Appl. Phys. 125 (2019) 035303.

[53] B. Xu, T. Feng, M. T. Agne, L. Zhou, X. Ruan, G. J. Snyder, Y. Wu, Highly porous thermoelectric nanocomposites with low thermal conductivity and high figure of merit from large-scale solution-synthesized $Bi_2Te_{2.5}Se_{0.5}$ hollow nanostructures, Angew. Chem. Int. Ed. 129 (2017) 3600-3605.

[54] H. Hu, H. L. Zhuang, Y. Jiang, J. Shi, J. W. Li, B. Cai, Z. Han, J. Pei, B. Su, Z. H. Ge, B. P. Zhang, J. F. Li, Thermoelectric $Cu_{12}Sb_4S_{13}$-based synthetic minerals with a sublimation-derived porous network, Adv. Mater. 33 (2021) e2103633.

[55] R. Gupta, B. Dongre, C. Bera, J. Carrete, The effect of Janus asymmetry on thermal transport in SnSSe, J. Phys. Chem. C 124 (2020) 17476-17484.

Graphical Abstract

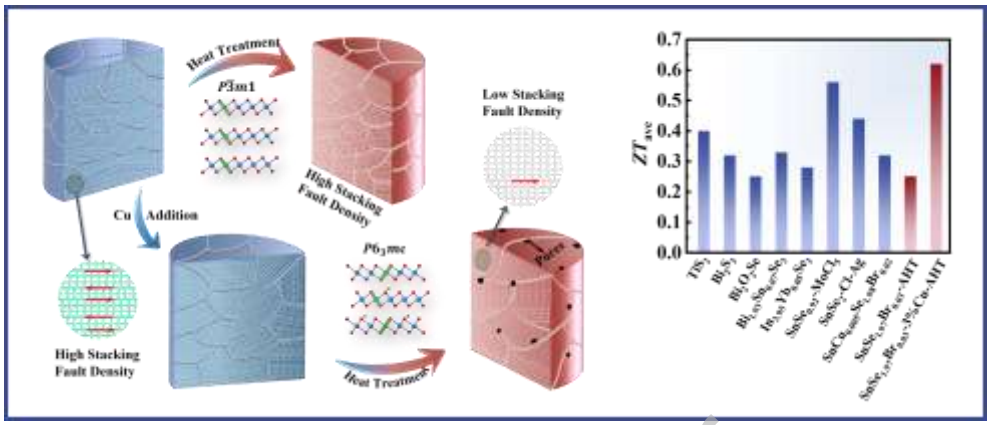

A new phase (SG $P6_3mc$) of $SnSe_2$ with a larger stacking fault formation energy can be formed by the addition of Cu, which leads to significantly reduced stacking fault density and thereby increased carrier mobility after heat treatment, finally resulting in a record ZT_{ave} value among *n*-type polycrystalline layered TE materials working in mediate-to-high temperature region.

Declaration of Competing Interest

The authors declare that they have no known competing financial interests or personal relationships that could have appeared to influence the work reported in this paper.